Full paper

Multi-band middle-infrared-compatible camouflage with thermal management via simple photonic structures

Meiyan Pan [a,1], Yun Huang [a,1], Qiang Li [a,*], Hao Luo [a], Huanzheng Zhu [a], Sandeep Kaur [a], Min Qiu [b,c]

[a] State Key Laboratory of Modern Optical Instrumentation, College of Optical Science and Engineering, Zhejiang University, Hangzhou, 310027, China
[b] Key Laboratory of 3D Micro/Nano Fabrication and Characterization of Zhejiang Province, School of Engineering, Westlake University, 18 Shilongshan Road, Hangzhou, 310024, China
[c] Institute of Advanced Technology, Westlake Institute for Advanced Study, 18 Shilongshan Road, Hangzhou, 310024, China

ABSTRACT

Perpetual advancements in modern detection technologies have augmented the need of multi-band (such as laser radar, visual) middle-infrared (MIR) compatible camouflage; however, its development is impeded by incompatible structural requirements of different camouflage effects and thermal challenge. This study demonstrates two simple photonic structures (Designs I and II) for visual and MIR camouflage with thermal management utilizing thin-film interference. The additional laser camouflage is realized by further incorporating simple wavelength-scale grating structures in Design I (Design II). The fabricated structures exhibit dual-band MIR camouflage by low emission ($\bar{\varepsilon}_{3-5\mu m} = 0.25$ and $\bar{\varepsilon}_{8-14\mu m} = 0.33$), radar camouflage to CO_2 laser by high absorption at 10.6 μm ($\alpha_{10.6\ \mu m} = 0.90$), visual camouflage by structural colors and thermal management by high emission in 5–8 μm band ($\bar{\varepsilon}_{5-8\mu m} = 0.77$). This study provides a guideline on coordinated control of electromagnetic wave and heat through simple structural design, thus has broad implications in energy harvesting and thermal information processing.

1. Introduction

Camouflage technologies involve achieving low observability in visible, mid-infrared (MIR), and radar spectra by color control [1,2], infrared signature modulation [3,4], and reflection suppression [5,6], respectively. In particular, MIR camouflage has attracted increasing interest owing to the extensive use of homing system that use MIR signal to search for and track target. According to the Stefan-Boltzmann law, the intensity of the MIR signal emitted from an object is proportional to the surface emissivity (ε) and the fourth power of its absolute temperature (T). Therefore, controlling the temperature and the surface emissivity are the two means to achieve MIR camouflage. The temperature control is a direct but difficult way because it requires additional cooling and heating devices [7–14]. By contrast, controlling the surface emissivity is an easier way as covering a low-emissive material on the object can efficiently suppress the MIR signal [15–23]. Traditional MIR

camouflage materials are metals that have ultra-broadband low emissivities in MIR wavelengths. However, modern detecting technologies have developed multi-band (such as laser radar, visual) detection capabilities for better object identification [24,25]. The traditional MIR camouflage materials fail at laser radar and microwave radar camouflage due to high reflection. Furthermore, their ability to control the MIR signal may be hindered by heat challenge due to internal and external heat sources (e.g. absorption of radar energy). Hence, advanced multi-band MIR-compatible camouflage technology with thermal management is desirable.

Achieving multi-band MIR-compatible camouflage with thermal management requires: (i) low emissivities in the dual-band MIR (3–5 μm mid-wavelength-infrared (MWIR) and 8–14 μm long-wavelength-infrared (LWIR)); (ii) high absorptivities at radar working wavelengths (such as 10.6 μm CO_2 laser radar); (iii) structural colors in visible spectra; and (iv) a high emissivity in the 5–8 μm band for efficient heat

dissipation [26–32]. Therefore, multi-band MIR-compatible camouflage is challenging as the spectral requirements for different bands vary or even conflict with each other. For example, the LWIR camouflage requires a low emissivity in 8–14 μm, which collides with the CO_2 laser camouflage requiring a high absorptivity at 10.6 μm. Previously, one-dimensional photonic crystals (1D-PCs) have been proposed for multi-band MIR compatible camouflage [33–35]. The spectra of the 1D-PCs are reported while their MIR camouflage performance is not demonstrated. The 1D-PCs also suffer from large thickness and bulkiness, leading to increased cost and poor mechanical stability. Metasurfaces have also been probed for multi-band MIR compatible camouflage with thermal management in some simulation studies [36, 37] and few experimental investigations [38,39]. In their experimental demonstrations, the metallic metasurfaces with magnetic resonances are exploited for thermal management [38,39]. The metasurfaces require subwavelength units, thereby complicating the fabrication; besides, they do not provide camouflage to laser radars. Thereby, using simple photonic structures for realizing multi-band MIR-compatible camouflage with thermal management remains a challenge.

In this study, two simple photonic structures (Designs I and II) for multi-band camouflage with thermal management have been proposed. Both designs utilize film interference to offer the challenging compatibility for dual-band MIR camouflage and thermal management. The additional laser camouflage to CO_2 laser in Design II is realized by further incorporating wavelength-scale grating structures. The introduced narrow-band grating mode can manipulate the trade-off condition for LWIR band camouflage (low emission) and laser camouflage (high absorption at 10.6 μm). These simple photonic structures present several distinctive advantages: (i) dual-band MIR and visual camouflage for both designs, and additional CO_2 laser radar camouflage for Design II; (ii) efficient thermal management by radiation in the 5–8 μm band and (iii) simple design that eases the device fabrication as the designs involves film (Design I) and wavelength-scale grating (Design II). The multi-band MIR-compatible camouflage with thermal management ability of our designs is demonstrated by that the fabricated sample blends objects into the background from IR cameras, absorbs the power of CO_2 laser, shows structural colors in visible images, and presents lower temperature than the conventional metal surface.
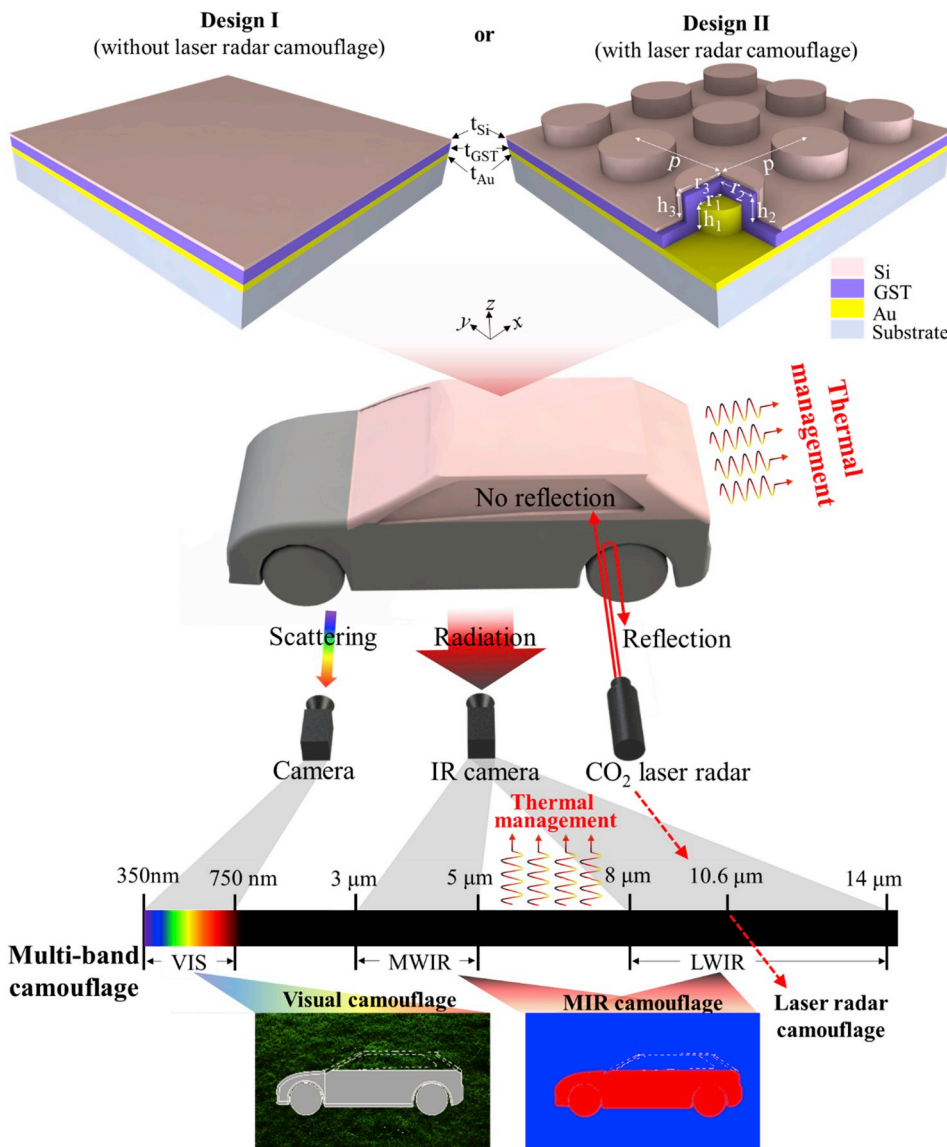

Fig. 1. Concept of multi-band MIR-compatible camouflage and thermal management. The upper body of a car surface is covered with the designed photonic structures (Designs I or II). They both hide the upper body from visible and MIR cameras, blending it into the environment. The thermal radiative flux in the 5–8 μm band that helps efficient cooling is beyond the MIR detection range. The additional feature of Design II is the laser radar camouflage (to CO_2 laser radar) by absorbing the incident light. The upper is schematics of the two designs. Design I contain Au, GST, and Si films of thicknesses of 200 nm, 220 nm, and 30 nm, respectively. Design II is comprised of two-dimensional lattice of Au micro-disks coated with the same GST and Si films. The other geometric parameters of Design II are: $h_1 = h_2 = h_3 = 0.8$ μm, $r_1 = 2.65$ μm, $r_2 = 2.87$ μm, $r_3 = 2.9$ μm, and $p = 10.1$ μm.

2. Results

2.1. Design and simulations

The conceptual features of the designed structures are pictorially depicted by shrouding the upper part of a car (Fig. 1). Both Design I and Design II can efficiently conceal the image from visible (by structural colors) and MIR (by signal suppression in the MWIR and LWIR bands) cameras. Design II can also absorb the light from CO_2 laser and thus offers camouflage to CO_2 laser radar. On the contrary, the remaining part of the car is unambiguously detected by visible and MIR cameras, as well as by the reflection of light from a CO_2 laser radar. Furthermore,

efficient thermal management in both designs is realized through selective radiation in the 5–8 μm band.

Design I comprises of successive deposition of thin films of Au, crystalline $Ge_2Sb_2Te_5$ (GST), and Si from bottom to top. The crystalline GST is a lossy material with a high refractive index (~6.2) in the MIR, enabling reduced thickness and strong absorption in thin-film interference. The thicknesses of Au and Si films are set as $t_{Au} = 200$ nm and $t_{Si} = 30$ nm, respectively. To provide a thin-film destructive interference (anti-reflection resonance) for high absorption/emission in the 5–8 μm band, the thickness of GST is set as 220 nm. Design II contains a two-dimensional lattice of Au micro-disks coated with the same GST and Si films as in design I. To form a strong grating mode at 10.6 μm, the radius
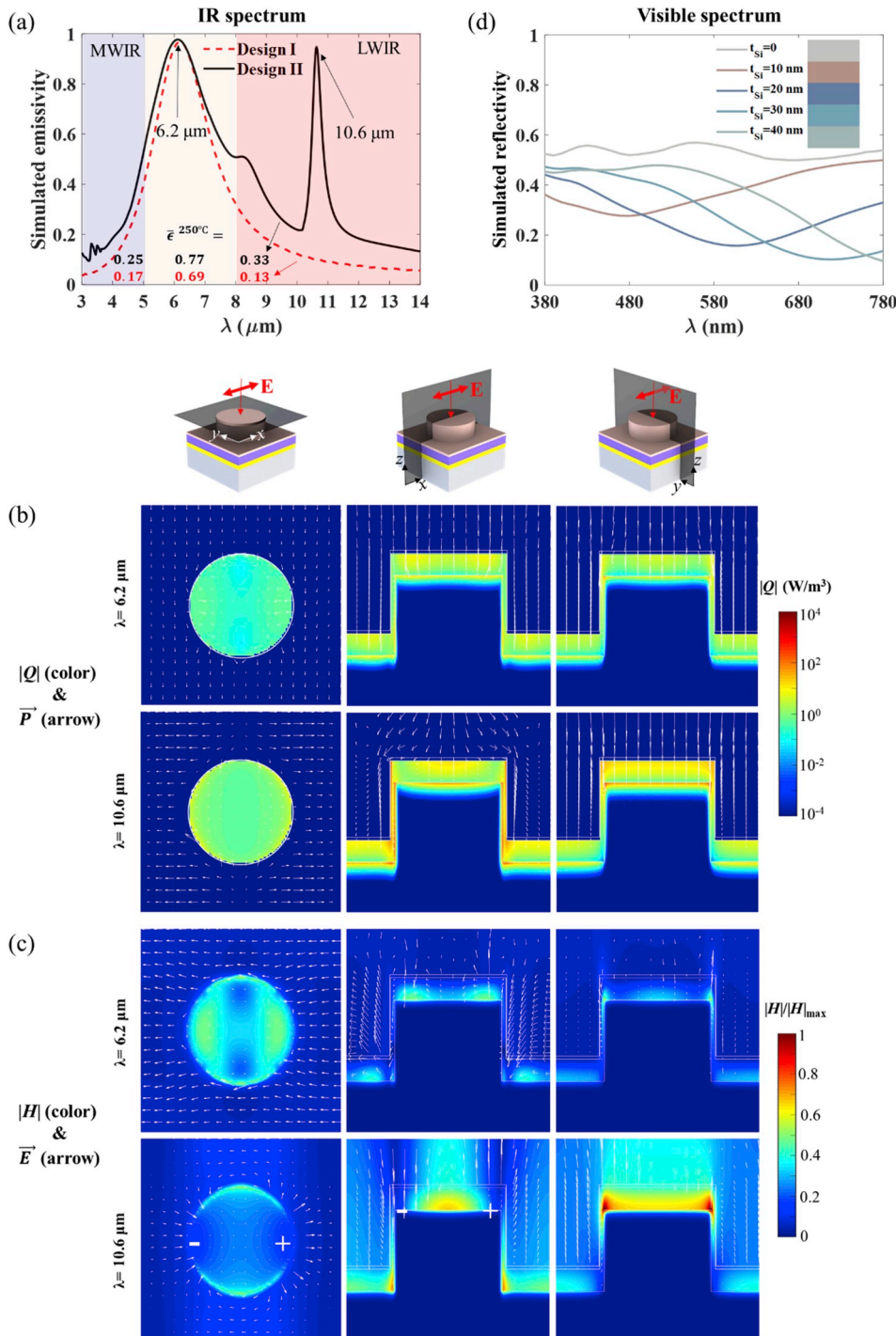

Fig. 2. a) Simulated spectral emissivity at normal incidence. b) Resistive loss (color) and Poynting vector (arrow) in the indicated xy-, xz- and yz-cross sections at the two peak wavelengths. c) Magnetic field intensity (color) and electric field (arrow) in the indicated xy-, xz- and yz-cross sections at the two peak wavelengths. d) Simulated reflection spectra in the visible regime for different Si thicknesses. Inset is the calculated colors corresponding to the thicknesses of the Si. The incident wave is x-polarized in the simulation. (For interpretation of the references to colour in this figure legend, the reader is referred to the web version of this article.)

(r_1) and height (h_1) of the gold disk are set at 2.65 μm and 0.8 μm, respectively, and the period of the lattice (p) is about 10.1 μm. Other parameters of design II are: $r_2 = r_1 + t_{GST} = 2.87$ μm, and $r_3 = r_2 + t_{si} = 2.9$ μm.

The absorption/emission and reflection responses of the two designed structures are numerically calculated using finite-difference-time-domain (FDTD) simulation (Fig. 2, details in Material and methods). The average emissivity $\overline{\varepsilon}$ for a wavelength band [λ_1 λ_2] at temperature T can be expressed in terms of spectral emissivity $\varepsilon(\lambda)$ and blackbody radiation $I_{BB}(\lambda, T)$ as:

$$\overline{\varepsilon}_{[\lambda_1 \, \lambda_2]} = \int_{\lambda_1}^{\lambda_2} \varepsilon(\lambda) I_{BB}(\lambda, T) d\lambda \, \Big/ \, \int_{\lambda_1}^{\lambda_2} I_{BB}(\lambda, T) d\lambda. \tag{1}$$

where $I_{BB}(\lambda, T) = hc^2/\lambda^5 \cdot [\exp(hc/\lambda k_B T) - 1]^{-1}$. The two designs both exhibit low average emissivities in the MWIR and LWIR bands. The calculated average normal emissivity $\overline{\varepsilon}$ or design I (II) at 250 °C is 0.17 (0.25) in the MWIR band, and 0.13 (0.33) in the LWIR band (Fig. 2a). Note that the average emissivities in these two bands are low at any temperature (blue and red lines in Fig. S8). The low value of the average emissivity $\overline{\varepsilon}$ is related to the designed GST thickness that supports no resonance within these bands.

Additionally, a high average emissivity is obtained in the 5–8 μm band, which is virtually not useable for most MIR cameras because of the high atmospheric absorption. The average emissivities of Design I and II in the 5–8 μm band are $\overline{\varepsilon}_I = 0.69$ and $\overline{\varepsilon}_{II} = 0.77$, with both peak emissivities close to unity at 6.2 μm wavelength (Fig. 2a and Fig. S1a). The optical spectra of the two designs are similar (except an additional 10.6 μm absorption) because they both come from the destructive interference in a single thin-film [40] which is established by the accumulation of heat and electromagnetic field distribution in the GST film (Fig. 2b (top) and Fig. 2c (top)). The emission spectrum is found to be almost independent of both the observation and polarization angles (Fig. S1b and Fig. S2a), indicating that dual-band MIR camouflage and radiative cooling are both highly omnidirectional.

For design II, the extra sharp absorption at 10.6 μm possesses the advantage of achieving camouflage for CO$_2$ laser radar, while simultaneously keeping the low average emissivity in the LWIR band. Such sharp absorption arises from the grating mode [41], which is implied by the horizontal energy flow along the structure (Fig. 2b (bottom)). Also, excited electric dipoles localizing the electromagnetic field can be seen (Fig. 2c (bottom)). The absorption peak at 10.6 μm is angle-dependent (Fig. S2a). Only normal absorption is required for laser radar camouflage as the oblique incidence of the laser light would be reflected to other directions which are beyond the detection of laser radar. Furthermore, the independence of the normal absorption on the polarization (Fig. S2b) indicates high robustness of design II to laser radar camouflage for different polarizations. Besides, the high absorptivity can hardly affect the temperature of design II as the absorbed energy is low due to the beam divergence [42].

The anti-reflective resonance (destructive interference) in the top silicon film is used to obtain different colors of the visible spectra (determined through the CIE color model [43]). The visual color is controlled by the silicon film thickness. As the top silicon film is much thinner than the radiation wavelengths, it is transparent to the thermal radiation wavelengths and thereby does not affect the infrared emissivity. The reflection dip in the visible spectrum red-shifts with the increasing silicon thickness (Fig. 2d), thus enabling visual camouflage with the selected colors. For instance, the corresponding colors with silicon thicknesses of 30 nm and 40 nm have the potential for visual camouflage in forests, and a 20 nm-thick Si film can be applied to visual camouflage in deserts.

Since the optical properties of Designs I and II are highly similar (except the additional absorption at 10.6 μm for Design II), only the experimental results of design II will be demonstrated in the following sections (Analysis and experimental results for Design I is included in Supplementary material Section S1).

2.2. Device and optical measurement

To verify the multi-band (dual-band MIR, laser radar and visual) camouflage and thermal management properties of the designed photonic structure, two samples for Design II with different Si film thicknesses (30 nm and 20 nm) are shown in Fig. 3a (see Material and methods for fabrication process). The visual colors are in accordance with the corresponding calculated colors (Inset in Fig. 2d). The geometry and the size of the fabricated structure are also consistent with the design (Fig. 3b and c). To ease the fabrication further, the grating is fabricated by covering the photoresist array with the gold film. The photoresist inside the Au disk does not affect the sample performance as the gold film thickness is larger than the penetration depth of IR light (about 29 nm for both 6.2 μm and 10.6 μm wavelengths).

The spectral emissivity and absorptivity of Sample A are measured by a Fourier-transform infrared (FTIR) spectrometer and a constructed optical path with a CO$_2$ laser as the source (details in Material and methods and Fig. S5). The normal absorptivity at 10.6 μm is measured as ~0.90, which is in accordance with the calculated value (0.92) (Fig. 3d). In the emission measurement, the IR spectra are measured at 250 °C for an enhanced signal-noise-ratio. The spectral emissivity $\varepsilon(\lambda)$ is not sensitive to absolute temperature T as long as it is below the melting temperature of GST (~600 °C [44]). The measured average emissivities $\overline{\varepsilon}$ at 250 °C (absorptivities α) in the MWIR, 5–8 μm, and LWIR bands are 0.56 (0.69), 0.73 (0.72), and 0.33 (0.27), respectively. For the 5–8 μm band, where the high emissivities are omnidirectional, the measured absorption (blue line) and emission (red line) are consistent with the simulated spectrum (black dash line). For the MWIR band, the actual absorption should be much smaller than the shown data as part of the incident light is scattered to directions beyond the collecting angles ([10° 20°]) [45]. Meanwhile, the measured emissivity of the design II sample in the MWIR band is higher than the actual value of the fabricated sample due to the large noise below 4 μm wavelength. For the LWIR band, the difference between the measured and simulated spectra at 10.6 μm can be interpreted by the dependence of measured data on the range of collecting angle range Θ (detailed in Supplementary material Section S2).

To evaluate the overall performance of our designed photonic structure, a factor using measured data could be defined as:

$$OP = \frac{P_{5-8\mu m}^2}{P_{MWIR} \cdot P_{LWIR}} \cdot \frac{\alpha_{10.6\mu m}}{\overline{\varepsilon}_{LWIR}} \tag{2}$$

where the P_{MWIR}, $P_{5-8\mu m}$, and P_{LWIR} represent the radiation energy in the MWIR, the 5–8 μm and the LWIR band, respectively; $\alpha_{10.6 \, \mu m}$ represents the absorption at 10.6 μm; $\overline{\varepsilon}_{LWIR}$ represents the average emissivity in the LWIR band. A high OP value can be obtained for a device with low emissivities in the MWIR and LWIR bands, high absorption at the working wavelength of CO$_2$ laser radar, and high radiative cooling efficiency. The overall performance of sample A (Fig. 3e) is compared with that of a conventional Au film and a reported 1D-PC with simultaneous MIR and CO$_2$ laser camouflage [35]. The Au film shows comparatively low overall performance ($OP_{Au} \approx 3$ at any temperature) due to its low radiation energy in the 5–8 μm band (P_{MWIR}) and low absorption at 10.6 μm. The overall performance of the fabricated sample ($OP_{sample} = 50$ at 30 °C) is better than that of the reported 1D-PC ($OP_{PC} = 31$ at 30 °C) because of the higher average emissivity in the 5–8 μm band and higher absorptivity at 10.6 μm. As the temperature increases, the performances of both the fabricated sample and the reported PC decrease because their radiation energy in the MWIR band increases. The Design I and the reported metasurface in Ref. [38] are compared as they both show simultaneous dual-band MIR camouflage and thermal management and the results indicate better performance for Design I but with a much simpler design (Supplementary material Section S1).
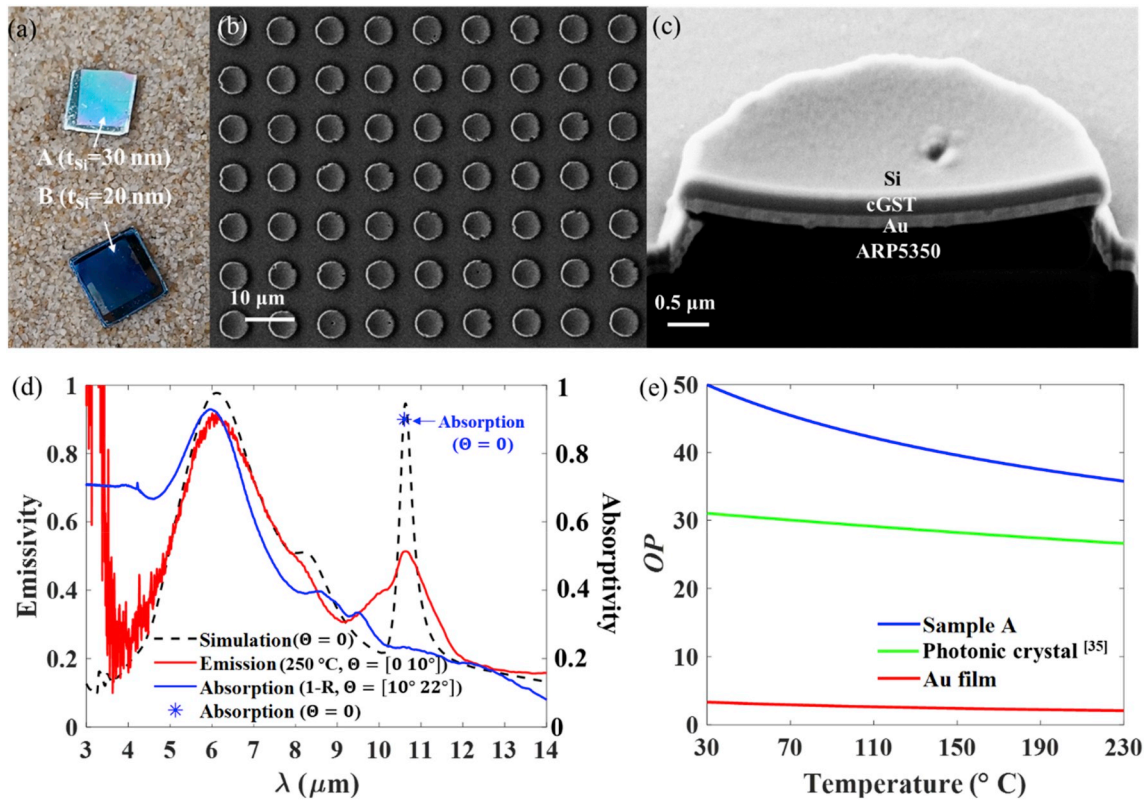
Fig. 3. a) Image of two samples with Si thicknesses of 30 nm (A) and 20 nm (B), respectively. b) Top-view and c) cutaway SEM images of Sample A. d) Spectral radiance of Sample A: simulated normal emissivity (black dash line), measured emissivity (red line) at 250 °C and absorptivity (blue line) by FTIR spectrometer, and the measured normal absorptivity at 10.6 μm (blue asterisk) by additionally constructed optical path. Θ represents the angle range that collects the incident/reflected/emissive waves. e) Evaluation of overall performance (*OP*) of multi-band (dual-band MIR and 10.6 μm laser radar) camouflage with thermal management effects for sample A, the reported 1D-PC [35] and the Au film. (For interpretation of the references to colour in this figure legend, the reader is referred to the web version of this article.)

2.3. Infrared camouflage demonstration

Most natural environments have an emissivity close to a blackbody. The "radiation temperature" (T_r) recorded by a MIR camera is related to the detected power (*P*) from the object and can be determined by the inverse function of $P(\varepsilon, T)$:

$$T_r = P^{-1}(\varepsilon_{IR}, T),\tag{3}$$

where ε_{IR} is the default emissivity (usually $\varepsilon_{IR} = 1$) in the IR camera; $P(\varepsilon, T)$ represents the power detected from the object surface, which includes the radiation intensity from the object (P_{rad}) and the reflection of ambient radiation by the object (P_{ref}) (Fig. 4a):

$$P(\varepsilon, T) = P_{rad}(\varepsilon, T) + P_{ref}(\varepsilon, \varepsilon_a, T_a)$$
$$= C\int_{\lambda_1}^{\lambda_2} \varepsilon(\lambda) \cdot \frac{hc^2}{\lambda^5} \left(e^{\frac{hc}{\lambda k_B T}} - 1 \right)^{-1} d\lambda + C\int_{\lambda_1}^{\lambda_2} [1 - \varepsilon(\lambda)] \cdot \varepsilon_a(\lambda) \cdot \frac{hc^2}{\lambda^5} \left(e^{\frac{hc}{\lambda k_B T_a}} - 1 \right)^{-1} d\lambda\tag{4}$$

where, $\varepsilon(\lambda)$ and $\varepsilon_a(\lambda)$ are the object's spectral emissivity and the ambient spectral emissivity, respectively; *T* is the object temperature; T_a is the ambient temperature; [λ_1, λ_2] is the working spectrum of the IR camera; *C* is the angle integral constant (detailed in Supplementary material Section S3). The relation is also suitable for a blackbody, whose reflection is zero because $\varepsilon(\lambda) = 1$.

The radiated and reflected power of the sample in the working wavelength band of our MIR camera (7.5 μm–14 μm) in both indoor and outdoor cases is calculated from the measured spectra (Fig. 4b and Fig. S7). The radiated power from the sample increases with the temperature but lower than a blackbody at the same temperature. For

instance, the radiated power at 150 °C from the sample (266.4 W/m^2) is about 35% of that from a blackbody (759.3 W/m^2). The detected power from the sample (sum of radiation and reflection) is smaller than the blackbody radiation in both indoor and outdoor cases. The reflected power is independent of the sample temperature and depends on the ambient spectral emissivity $\varepsilon_a(\lambda)$, ambient temperature T_a, and reflectivity (1- $\varepsilon(\lambda)$) of the sample. For the indoor case, $T_a = 20$ °C and $\varepsilon_a \approx 1$ as the surroundings can be regarded as blackbodies. For the outdoor case, the sample faces the cloudy sky and the radiation temperature of the cloud is measured to be −14.6 °C by the MIR camera (although the real T_a and ε_a are not measurable, the ambient radiation could be calculated from the radiation temperature of the cloud). Therefore, the amount of outdoor reflection is lower than the indoor reflection due to the lower ambient spectral emissivity $\varepsilon_a(\lambda)$ and ambient temperature T_a. At the ambient temperature, MIR power from the indoor object equals to blackbody radiation because of the compensation by the reflected power.

The radiation temperatures of the sample at different real temperatures are measured with a MIR camera (Fluke Ti10) in both indoor and outdoor cases (Fig. 4c). The measured data is in good agreement with the calculated results. In both cases, the measured radiation temperatures (T_r) of the sample are much lower than its real temperatures (*T*), and the radiation temperatures grow up with the increasing real temperatures. With the same real temperature, the radiation temperature in the outdoor case is always lower than that indoor because of the lower reflected ambient radiation as mentioned above. For example, with the real temperature $T = 40$ °C, the indoor and outdoor radiation temperatures of the sample are 27.9 °C and 9.5 °C, respectively.

For excellent MIR camouflage, the objects are "invisible" under the
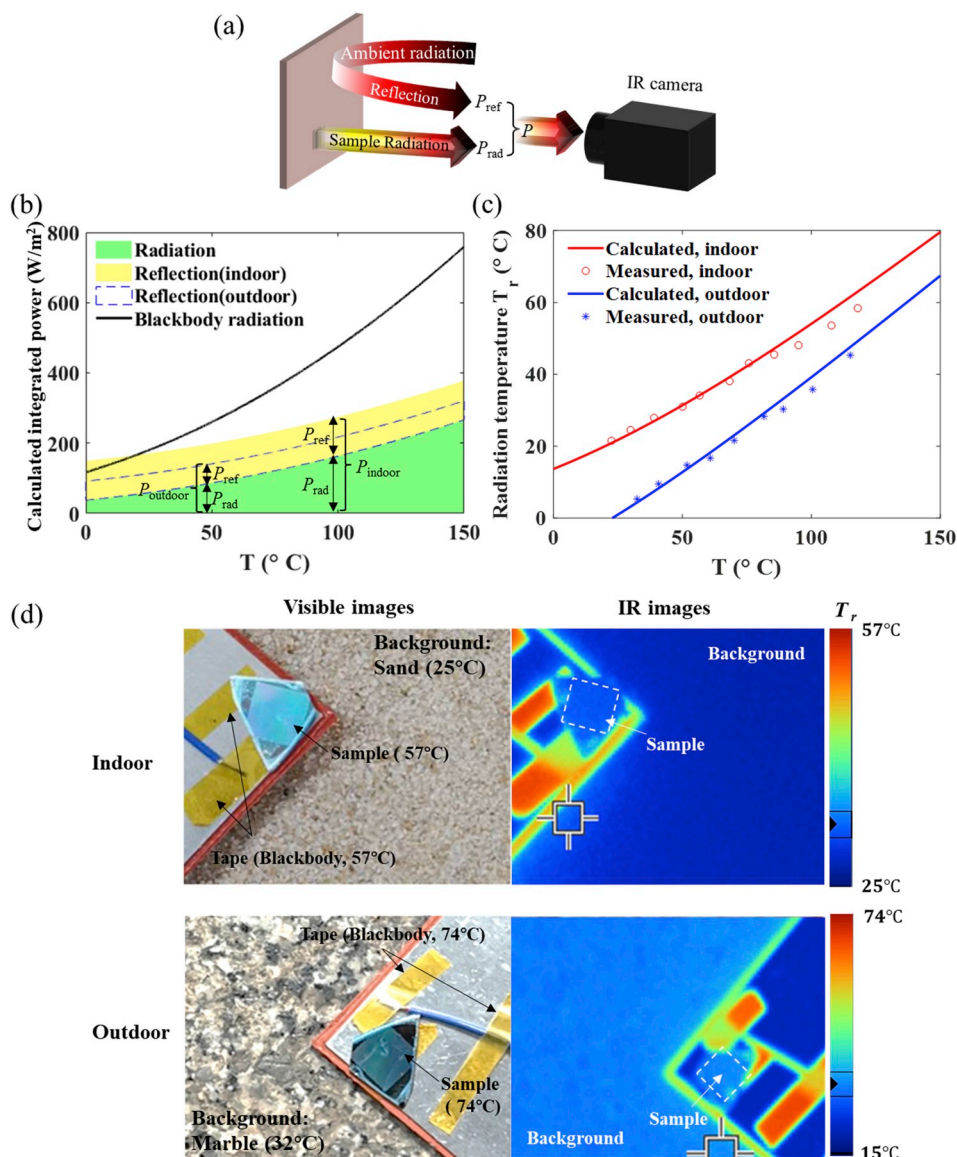
Fig. 4. a) Schematic of MIR power detected by the MIR camera (working band: 7.5 μm–14 μm). The MIR power from the sample contains the sample radiation and the reflected ambient radiation. b) The relation between sample temperature and its integrated power detected by the MIR camera. The power from the sample contains two parts: the sample radiation P_{rad} (green area) and the reflected environment radiation by the sample P_{ref}. The blue dash frame represents the indoor reflection while the yellow area accounts for the outdoor reflection. The black line represents the integrated power of a blackbody. The ambient temperature is 20 °C. c) The relation between radiation temperatures and real temperatures of the sample: the lines are calculated with the integrated power in b), and the dots are experimental data. d) Indoor (top) and outdoor (bottom) MIR camouflage demonstration of the sample. The left and right figures are visible and MIR images, respectively. The radiation temperatures of the sample are the same as that of the background in both cases. (For interpretation of the references to colour in this figure legend, the reader is referred to the web version of this article.)

MIR camera when their radiation temperatures match the background temperature (T_b). Such MIR camouflage effect of the fabricated sample is also experimentally demonstrated (Fig. 4d). For the indoor case (Fig. 4d (top left)), the sample and the tape are placed on a heat controller and

their temperature is at 57 °C and the background sand temperature (T_b = 25 °C) is same as ambient temperature. At the ambient temperature, the indoor object performs like a blackbody in the MIR camera. In the corresponding MIR image (Fig. 4d (top-right)), the sample appears same
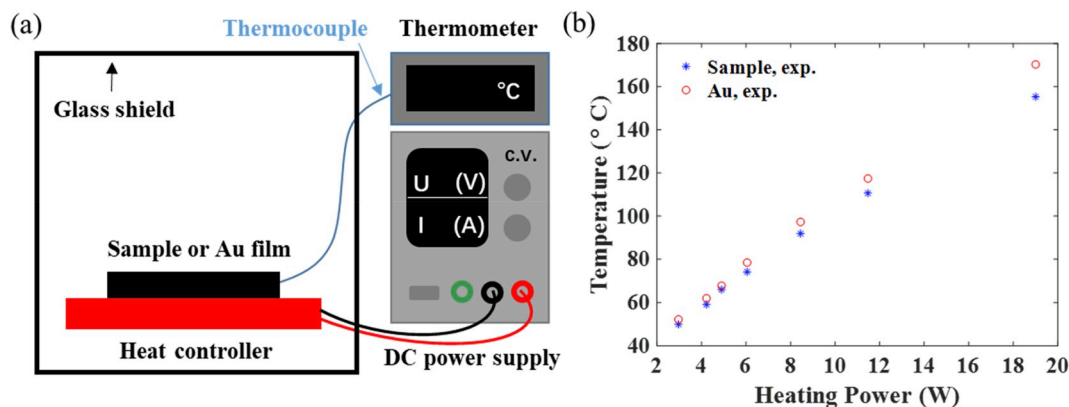

Fig. 5. a) Schematic of the experimental setup to measure the thermal management (cooling effect) of the designed photonic structure. b) The real temperature on the surface of the sample (blue asterisks) and the Au film (red circles). (For interpretation of the references to colour in this figure legend, the reader is referred to the web version of this article.)

as sand, since its radiation temperature ($T_r = 26\,°C$) is almost identical to that of sand ($T_b = 25\,°C$), while the tape (can be regarded as a black body) is thermally detected owing to its high radiation temperature ($T_r = 57\,°C \neq T_b$). Similarly, for the outdoor case, the ambient temperature is $26\,°C$ and a marble ground ($T_b = 32\,°C$, $\varepsilon = 0.95$) is used in the background (Fig. 4d (bottom left)). The IR image (Fig. 4d (bottom right)) reveals that the fabricated sample ($T = 74\,°C$) is also hidden into the background ($T_r = 32\,°C = T_b$), while the highly emissive tape with the same temperature is thermally detected.

2.4. Thermal management demonstration

The thermal management by radiative cooling is demonstrated by comparing the temperatures of the sample with an equal-sized and equally thin Au film. The heating energy is provided with a power supply, and the temperature is measured by a thermocouple connected to a thermometer. A glass shield is used to avoid air disturbance (Fig. 5a). To obtain MIR camouflage with fast response, a substrate with a small thickness and a low heat capacity should be used (see Supplementary material Section S6). The temperatures of both the sample and the Au film increase with increasing heating power. With the same heating power, the temperature of the sample is always lower than that of the Au film owing to thermal management by radiative cooling (Fig. 5b). For instance, with the heating power of 19 W, the real temperature of the sample (155.3 °C) is 15 °C lower than that of the Au film (170.3 °C). With the growing heating power, both the equilibrium temperatures of the sample and the Au film increase. As the average emissivity of the sample increases while that of the Au film is almost constant (Fig. S8), the temperature difference between them increases because of the increasingly larger radiation power from the sample than that from the Au film. The designed photonic structure possesses good thermal management performance especially at high temperatures.

3. Conclusion

In summary, multi-band MIR-compatible camouflage with thermal management is achieved via simple photonic structures. First, compared with the previous study using 1D-PCs and metasurfaces, the designs are much simpler and possess more challengingly compatible features (Table S1): the trilayer thin-film structure (Design I) offers simultaneous dual-band MIR camouflage, visual camouflage, and thermal management, while incorporating wavelength-scale grating structures in Design I (Design II) can provide CO_2 laser camouflage as well. Second, the designs have the potential to be compatible with radar camouflage for microwave spectrum with millimeter-scale patterning of the Au films and integration of a microwave absorber. Third, portable or wearable applications may be enabled if our designs are manufactured on the surface of a thermostable flexible substrate such as polyimide or polyethylene terephthalate films (Supplementary material Section S5). Last, this work provides a clue for coordinated control of multi-band electromagnetic wave and heat through simple structural design, thus has broad implications in energy harvesting and thermal information manipulation.

4. Material and methods

Sample fabrication: The sample (design II) was fabricated by photolithography technique (Fig. S3). For the fabrication of photoresist arrays, an 800 nm thick ARP5350 film was spun onto the silicon substrate and annealed for 5 min at 105 °C. Then the photoresist was patterned by photolithography using a double-sided mask aligner system (MA6–BSA). Afterwards, the sample was immersed in a developer (1:6 AR 300-26/ Deionized (DI) water) for 12 s followed by 1 min DI water rinse. After the development, a 200 nm thick Au thin film (thin enough to prevent the leakage of the radiation to the substrate side), a 220 nm thick GST thin film, and ultrathin Si film were successively deposited using high

vacuum magnetron sputtering technique at room temperature. Different thicknesses of Si were chosen for different colors. Finally, the samples were annealed at 180 °C for 4 min to transfer the GST layer from amorphous state to crystalline state.

Optical measurement: The spectral emission was measured by FTIR with a room-temperature doped triglycine sulfate detector. The samples were fixed on a temperature controller, and the emitted power was sent into the FTIR (Fig. S4a). The temperatures of both the black soot and the samples were measured at 250 °C to ensure high emitted power and to decrease the noise. The spectral absorption was measured by an FTIR microscope where the reflected light is collected (Fig. S4b). The spectral reflection of Au film was measured as the reference. The absorption at 10.6 μm was measured using a CO_2 laser (Synrad Firestar vi30) in which the output power has been controlled by a waveform generator (Feel-Tech FY6600). The normally reflecting light of the sample was extracted by a ZnSe beam splitter and collected by a power meter (LPE-1A) (Fig. S5). The reflected power of a 200 nm thick Au film was measured as the reference, with the average reflected power being 4.14 mW. Then the Au film was replaced with the sample A and the average value of the reflected power was measured as 0.41 mW. The infrared images were recorded by an IR camera (Fluke Ti10) with a spatial resolution of 500 μm, a spectral range 7.5–14 μm, and a temperature range from - 20 °C to 250 °C.

Numerical simulations: The simulations were performed with the FDTD Solutions v8.13, Lumerical software. The relative permittivity of gold, GST, and silicon was obtained from Ref. [18], Ref. [15], and Ref. [46], respectively. According to Kirchhoff's law of thermal radiation, the simulated emissivity can be replaced by the simulated absorptivity, and the observation angles can be replaced by the incident angles.

Declaration of competing interest

The authors declare that they have no known competing financial interests or personal relationships that could have appeared to influence the work reported in this paper.

Appendix A. Supplementary data

Supplementary data to this article can be found online at https://doi.org/10.1016/j.nanoen.2020.104449.

References

[1] J. Teyssier, S.V. Saenko, D. van der Marel, M.C. Milinkovitch, Photonic crystals cause active colour change in chameleons, Nat. Commun. 6 (2015) 6368, https://doi.org/10.1038/ncomms7368.
[2] J.H. Pikul, S. Li, H. Bai, R.T. Hanlon, I. Cohen, R.F. Shepherd, Stretchable surfaces with programmable 3D texture morphing for synthetic camouflaging skins, Science 358 (2017) 210–214, https://doi.org/10.1126/science.aan5627.
[3] O. Ilic, P. Bermel, G. Chen, J.D. Joannopoulos, I. Celanovic, M. Soljacic, Tailoring high-temperature radiation and the resurrection of the incandescent source, Nat. Nanotechnol. 11 (2016) 320–324, https://doi.org/10.1038/nnano.2015.309.

[4] Y. Li, X. Bai, T. Yang, H. Luo, C.-W. Qiu, Structured thermal surface for radiative camouflage, Nat. Commun. 9 (2018), https://doi.org/10.1038/s41467-017-02678-8.

[5] K. Iwaszczuk, A.C. Strikwerda, K. Fan, X. Zhang, R.D. Averitt, P.U. Jepsen, Flexible metamaterial absorbers for stealth applications at terahertz frequencies, Opt. Express 20 (2012) 635–643, https://doi.org/10.1364/oe.20.000635.

[6] B.W. Bai, X.P. Li, J. Xu, Y.M. Liu, Reflections of electromagnetic waves obliquely incident on a multilayer stealth structure with plasma and radar absorbing material, IEEE Trans. Plasma Sci. 43 (2015) 2588–2597, https://doi.org/10.1109/tps.2015.2447536.

[7] T.C. Han, X. Bai, J.T.L. Thong, B.W. Li, C.W. Qiu, Full control and manipulation of heat signatures: cloaking, camouflage and thermal metamaterials, Adv. Mater. 26 (2014) 1731–1734, https://doi.org/10.1002/adma.201304448.

[8] L. Xu, S. Yang, J. Huang, Passive metashells with adaptive thermal conductivities: chameleonlike behavior and its origin, Phys. Rev. Appl. 11 (2019), https://doi.org/10.1103/PhysRevApplied.11.054071.

[9] R. Hu, S.L. Zhou, Y. Li, D.Y. Lei, X.B. Luo, C.W. Qiu, Illusion thermotics, Adv. Mater. 30 (2018) 8, https://doi.org/10.1002/adma.201707237.

[10] T.C. Han, X. Bai, D.L. Gao, J.T.L. Thong, B.W. Li, C.W. Qiu, Experimental demonstration of a bilayer thermal cloak, Phys. Rev. Lett. 112 (2014) 5, https://doi.org/10.1103/PhysRevLett.112.054302.

[11] R. Schittny, M. Kadic, S. Guenneau, M. Wegener, Experiments on transformation thermodynamics: molding the flow of heat, Phys. Rev. Lett. 110 (2013) 5, https://doi.org/10.1103/PhysRevLett.110.195901.

[12] D.M. Nguyen, H.Y. Xu, Y.M. Zhang, B.L. Zhang, Active thermal cloak, Appl. Phys. Lett. 107 (2015) 4, https://doi.org/10.1063/1.4930989.

[13] C.Z. Fan, Y. Gao, J.P. Huang, Shaped graded materials with an apparent negative thermal conductivity, Appl. Phys. Lett. 92 (2008) 251907, https://doi.org/10.1063/1.2951600.

[14] L. Xu, J. Huang, Metamaterials for manipulating thermal radiation: transparency, cloak, and expander, Phys.Rev. Applied 12 (2019), 044048, https://doi.org/10.1103/PhysRevApplied.12.044048.

[15] Y.R. Qu, Q. Li, L. Cai, M.Y. Pan, P. Ghosh, K.K. Du, M. Qiu, Thermal camouflage based on the phase-changing material GST, Light: Sci. Appl. 7 (2018) 10, https://doi.org/10.1038/s41377-018-0038-5.

[16] L. Xiao, H. Ma, J. Liu, W. Zhao, Y. Jia, Q. Zhao, K. Liu, Y. Wu, Y. Wei, S. Fan, K. Jiang, Fast adaptive thermal camouflage based on flexible VO2/graphene/CNT thin films, Nano Lett. 15 (2015) 8365–8370, https://doi.org/10.1021/acs.nanolett.5b04090.

[17] M.A. Kats, R. Blanchard, S.Y. Zhang, P. Genevet, C.H. Ko, S. Ramanathan, F. Capasso, Vanadium dioxide as a natural disordered metamaterial: perfect thermal emission and large broadband negative differential thermal emittance, Phys. Rev. X 3 (2013) 7, https://doi.org/10.1103/PhysRevX.3.041004.

[18] Y.R. Qu, Q. Li, K.K. Du, L. Cai, J. Lu, M. Qiu, Dynamic thermal emission control based on ultrathin plasmonic metamaterials including phase-changing material GST, Laser Photonics Rev. 11 (2017) 6, https://doi.org/10.1002/lpor.201700091.

[19] C. Xu, G.T. Stiubianu, A.A. Gorodetsky, Adaptive infrared-reflecting systems inspired by cephalopods, Science 359 (2018) 1495–1500, https://doi.org/10.1126/science.aar5191.

[20] D. Costantini, A. Lefebvre, A.L. Coutrot, I. Moldovan-Doyen, J.P. Hugonin, S. Boutami, F. Marquier, H. Benisty, J.J. Greffet, Plasmonic metasurface for directional and frequency-selective thermal emission, Phys. Rev. Appl. 4 (2015) 6, https://doi.org/10.1103/PhysRevApplied.4.014023.

[21] X. Xie, X. Li, M.B. Pu, X.L. Ma, K.P. Liu, Y.H. Guo, X.G. Luo, Plasmonic metasurfaces for simultaneous thermal infrared invisibility and holographic illusion, Adv. Funct. Mater. 28 (2018) 6, https://doi.org/10.1002/adfm.201706673.

[22] Z. Wang, T.S. Luk, Y.X. Tan, D.X. Ji, M. Zhou, Q.Q. Gan, Z.F. Yu, Tunneling-enabled spectrally selective thermal emitter based on flat metallic films, Appl. Phys. Lett. 106 (2015) 5, https://doi.org/10.1063/1.4914886.

[23] K.-K. Du, Q. Li, Y.-B. Lyu, J.-C. Ding, Y. Lu, Z.-Y. Cheng, M. Qiu, Control over emissivity of zero-static-power thermal emitters based on phase-changing material GST, Light: Sci. Appl. 6 (2017), e16194, https://doi.org/10.1038/lsa.2016.194. https://www.nature.com/articles/lsa2016194#supplementary-information.

[24] C.T. Nguyen, J.P. Havlicek, G. Fan, J.T. Caulfield, M.S. Pattichis, in: Presented at 48th Asilomar Conference on Signals, Systems and Computers, Robust Dual-Band MWIR/LWIR Infrared Target Tracking, Pacific Grove, CA, 2014. Nov 02-05.

[25] R.E. Ball, The Fundamentals of Aircraft Combat Survivability: Analysis and Design, American Institute of Aeronautics and Astronautics, Place, Published, 2003.

[26] B. Bhatia, A. Leroy, Y. Shen, L. Zhao, M. Gianello, D. Li, T. Gu, J. Hu, M. Soljacic, E. N. Wang, Passive directional sub-ambient daytime radiative cooling, Nat. Commun. 9 (2018), https://doi.org/10.1038/s41467-018-07293-9.

[27] A.P. Raman, M.A. Anoma, L. Zhu, E. Rephaeli, S. Fan, Passive radiative cooling below ambient air temperature under direct sunlight, Nature 515 (2014) 540–544, https://doi.org/10.1038/nature13883.

[28] P.C. Hsu, A.Y. Song, P.B. Catrysse, C. Liu, Y.C. Peng, J. Xie, S.H. Fan, Y. Cui, Radiative human body cooling by nanoporous polyethylene textile, Science 353 (2016) 1019–1023, https://doi.org/10.1126/science.aaf5471.

[29] T. Li, Y. Zhai, S.M. He, W.T. Gan, Z.Y. Wei, M. Heidarinejad, D. Dalgo, R.Y. Mi, X. P. Zhao, J.W. Song, J.Q. Dai, C.J. Chen, A. Aili, A. Vellore, A. Martini, R.G. Yang, J. Srebric, X.B. Yin, L.B. Hu, A radiative cooling structural material, Science 364 (2019) 760, https://doi.org/10.1126/science.aau9101.

[30] E.A. Goldstein, A.P. Raman, S. Fan, Sub-ambient non-evaporative fluid cooling with the sky, Nat. Energy 2 (2017), https://doi.org/10.1038/nenergy.2017.143.

[31] P.C. Hsu, X.G. Liu, C. Liu, X. Xie, H.R. Lee, A.J. Welch, T. Zhao, Y. Cui, Personal thermal management by metallic nanowire-coated textile, Nano Lett. 15 (2015) 365–371, https://doi.org/10.1021/nl5036572.

[32] Z. Chen, L. Zhu, W. Li, S. Fan, Simultaneously and synergistically harvest energy from the sun and outer space, Joule 3 (2019) 101–110, https://doi.org/10.1016/j.joule.2018.10.009.

[33] H. Hogstrom, G. Forssell, C.G. Ribbing, Realization of selective low emittance in both thermal atmospheric windows, Opt. Eng. 44 (2005) 1–7, 7.

[34] L. Peng, D. Liu, H. Cheng, S. Zhou, M. Zu, A multilayer film based selective thermal emitter for infrared stealth technology, Adv. Opti. Mat. 6 (2018) 1801006, https://doi.org/10.1002/adom.201801006.

[35] J.-K. Zhang, J.-M. Shi, D.-P. Zhao, Q.-C. Wang, C.-M. Wang, Realization of compatible stealth material for infrared, laser and radar based on one-dimensional doping-structure photonic crystals, Infrared Phys. Technol. 85 (2017) 62–65, https://doi.org/10.1016/j.infrared.2017.05.018.

[36] L. Zhao, H. Liu, Z. He, S. Dong, All-metal frequency-selective absorber/emitter for laser stealth and infrared stealth, Appl. Opt. 57 (2018) 1757–1764, https://doi.org/10.1364/AO.57.001757.

[37] J. Kim, K. Han, J.W. Hahn, Selective dual-band metamaterial perfect absorber for infrared stealth technology, Sci. Rep. 7 (2017) 6740, https://doi.org/10.1038/s41598-017-06749-0.

[38] N. Lee, T. Kim, J.-S. Lim, I. Chang, H.H. Cho, Metamaterial-selective emitter for maximizing infrared camouflage performance with energy dissipation, ACS Appl. Mater. Interfaces 11 (2019) 21250–21257, https://doi.org/10.1021/acsami.9b04478.

[39] T. Kim, J.Y. Bae, N. Lee, H.H. Cho, Hierarchical metamaterials for multispectral camouflage of infrared and microwaves, Adv. Funct. Mater. 29 (2019) 8, https://doi.org/10.1002/adfm.201807319.

[40] M.A. Kats, F. Capasso, Optical absorbers based on strong interference in ultra-thin films, Laser Photonics Rev. 10 (2016) 735–749, https://doi.org/10.1002/lpor.201600098.

[41] L. Meng, D. Zhao, Z. Ruan, Q. Li, Y. Yang, M. Qiu, Optimized grating as an ultra-narrow band absorber or plasmonic sensor, Opt. Lett. 39 (2014) 1137–1140, https://doi.org/10.1364/OL.39.001137.

[42] H.M. Lamberton, V.G. Roper, Beam divergence of a highly multimode CO2 laser, J. Phys. E Sci. Instrum. 11 (1978) 1102–1103, https://doi.org/10.1088/0022-3735/11/11/007.

[43] K. McLaren, The development of the CIE 1976 (L* a* b*) uniform colour space and colour-difference formula, J. Soc. Dye. Colour. 92 (1976) 338–341, https://doi.org/10.1111/j.1478-4408.1976.tb03301.x.

[44] S. Raoux, T.J. Ibm, in: Y. Nishi (Ed.), Advances in Non-volatile Memory and Storage Technology, Woodhead Publishing, 2014, pp. 161–199, https://doi.org/10.1533/9780857098092.2.161.

[45] M.G. Moharam, T.K. Gaylord, Rigorous coupled-wave analysis of planar-grating diffraction, 71, 1981, pp. 811–818, https://doi.org/10.1364/josa.71.000811.

[46] E.D. Palik, in: E.D. Palik (Ed.), Handbook of Optical Constants of Solids, Academic Press, Burlington, USA, 1997, pp. 5–114.

Meiyan Pan received the B.Sc. degree from South China Normal University, Guangzhou, China, in the year 2015. She is now a Ph.D. student in Laboratory of Integrated Photonics and Nanophotonics, Zhejiang University. Her research interest focuses on multiband optical camouflage and thermal management for objects with high temperature.

Yun Huang received the B.Eng. degree from Zhejiang University, Hangzhou, China, in 2017. He is now a Ph.D. student in Laboratory of Integrated Photonics and Nanophotonics, Zhejiang University. His research interest focuses on coupled-mode-theory based optics, flexible and adjustable optical devices, and their application in infrared range.

Prof. Qiang Li received the B.Sc. degree and M. Eng from the Harbin Institute of Technology, Harbin, China, in 2005 and 2007, respectively. He obtained the Ph.D. degree in Microelectronics and Applied Physics from the Royal Institute of Technology (KTH), Stockholm, Sweden, in 2011. In 2011 he joined College of Optical Science and Engineering, Zhejiang University, as an assistant professor. He became an associate professor in 2013 and a full professor in 2017. His research interest focuses on energy-efficient silicon-/metal-based optoelectronic materials, devices and their applications in optical communications and energy utilization.
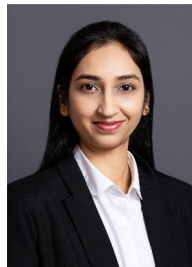
Dr. Sandeep Kaur received her Ph.D. degree from Chonbuk National University, South Korea in 2018. She is currently a post doctorate fellow at the College of Optical Science and Engineering, Zhejiang University, China. Her current research includes personal thermal management and textile integrated microelectronic devices.

Hao Luo received the B.Sc. degree from Zhejiang University, Hangzhou, China, in 2016. He also obtained honors degrees of Chu Kechen Honors College in Zhejiang University. He is now a visiting student in Prof. Harish Bhaskaran's group in the University of Oxford. His research interest focuses on cost-effective personal thermal management and nanophotonic devices incorporating phase-change chalcogenides.

Prof. Min Qiu received the Ph.D. degree in Physics from Zhejiang University, China in 1999. He became an assistant professor and a full professor at the Royal Institute of Technology (KTH), Sweden, in 2001 and 2009, respectively. Since 2010, he worked as a professor at Zhejiang University. He was the Director of State Key Laboratory of Modern Optical Instrumentation, Zhejiang University. In 2018 he joined Westlake University as a Chair Professor of Photonics and Vice President for Research. His research interests include nanofabrication technology, nanophotonics, and green photonics.
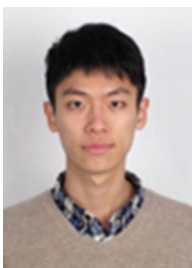
Huanzheng Zhu received the B.Sc. degree from Zhejiang University, Hangzhou, China, in 2016. He also obtained honors degrees of Chu Kechen Honors College in Zhejiang University. He is now a Ph.D. student in Laboratory of Integrated Photonics and Nanophotonics, Zhejiang University. His research interest focuses on multiband optical camouflage and thermal management for objects with high temperature.